# Pulse-Shortening in a Relativistic Magnetron: The Role of Anode Block Axial Endcaps

John G. Leopold, Anatoli S. Shlapakovski, Arkady F. Sayapin, and Yakov E. Krasik

***Abstract*— A six-vane relativistic magnetron with a single radial output slot is studied by 3-D particle in cell simulations without the presence of plasma. We find that when the six radial slots in the anode block are closed at their axial ends by conducting endcaps, the power flow behaves in a way different from that when they are not. When there are no endcaps, microwave power pulse-shortening is the result of the magnetron impedance being undermatched to the pulsed-power generator, and it cancels when the magnetron impedance is increased sufficiently. The axial electron current flowing in the downstream cavity reduces to negligible values and plays no part in the power flow. When anode block endcaps are added, this axial leakage current is significant and the downstream cavity acts as a second load attached in parallel to the magnetron. For pulse-shortening to cancel, the magnetron impedance needs to increase, which can be achieved by reducing the downstream axial section impedance. We demonstrate this by increasing the axial current. Between the parameter regions where pulse-shortening exists and where it does not, there is a metastable transition region where there is mode competition resulting in a beating pattern separating two regions each characterized by a single mode.**

***Index Terms*— Magnetron, microwave, power flow, pulse-shortening, relativistic.**

## I. Introduction

RADIATION power pulse-shortening is found to be inherent to most high-power microwave devices based on power extraction from high-current electron beams. Considerable effort has been invested in attempts to alleviate this shortcoming in relativistic magnetrons. Relativistic magnetrons have first been studied in the 1970s [1], modelled by particle in cell (PIC) simulations [2]–[6], and experimentally investigated in various configurations ever since [7]–[18]. The accepted explanation of pulse-shortening is cathode plasma formation followed by plasma expansion toward the anode within the electromagnetic interaction region [19]. Although some modelling work has pointed out situations where pulse-shortening occurs without the presence of plasma [20], [21], the mechanism responsible for this has not yet been fully understood. In experiments performed in our laboratory, no plasma expansion was observed across the cathode–anode gap within the first ∼100 ns [22], yet circumstances of pulse-shortening were detected.

Manuscript received March 27, 2016; revised May 29, 2016; accepted June 11, 2016. Date of publication June 24, 2016; date of current version August 9, 2016.

The authors are with the Department of Physics, Technion–Israel Institute of Technology, Haifa 32000, Israel (e-mail: leopoldjg@ph.technion.ac.il; shl@physics.technion.ac.il; sayapin@physics.technion.ac.il; fnkrasik@physics.technion.ac.il).

Color versions of one or more of the figures in this paper are available online at http://ieeexplore.ieee.org.

Digital Object Identifier 10.1109/TPS.2016.2580613

Recently, we have used 3-D PIC simulations to study a six-vane, single radial output, and six axially open slot cavity relativistic magnetron [23]. It was found that for certain values of the cathode diameter and the size of the electron emitting area, the electron current to the anode is higher than that supportable by the constant generator voltage. In other words, when the magnetron impedance becomes undermatched relative to the generator impedance, the voltage amplitude applied to the magnetron decreases resulting in a decrease in the azimuthal drift current, which causes the radiation power to drop. We have demonstrated that to cancel microwave power pulse-shortening, the magnetron impedance needs to be increased. To increase the magnetron impedance, we decreased the emitted current by reducing the size of the emission area [23] or the cathode radius [24]. The important role of the generator impedance was recognized early on but not studied in detail [20], [25].

In this paper, we report our findings for the same magnetron but with all its six slots covered by conducting endcaps at both axial ends of the anode block. As the magnetically insulated electron beam rotates around the axis, voltage differences are generated between the edges of the slots. With endcaps, these edges are shorted making the two devices different in their electric field spatial distribution, and therefore, it should not be surprising that these magnetrons behave in a different manner.

We have been able to understand the mechanism responsible for pulse-shortening for this system within a framework similar to that shown before [23], [24]. This system is more complex than when there are no anode endcaps but impedance mismatch and power flow are most important.

We use the MAGIC 3-D PIC code [26] to study this relativistic magnetron. Our work so far has not addressed the question of improving the efficiency of these devices but we believe that a better understanding of the power flow and electron beam dynamics will ultimately help us in understanding the efficiency-limiting factors too.

## II. Geometry and the Simulation Method

The geometry of the six-vane single radial output relativistic magnetron studied in this paper is shown in Fig. 1. An $[x, y]$ cross section perpendicular to the $z$-axis at $z = 0$ is seen in Fig. 1(a)–(c). A conical antenna extends from one of the resonator cavities, which is open through an iris [slot s5 in Fig. 1(a)]. Fig. 1(d) and (e) is $[r, z]$ cross sections at polar angles within a closed cavity and a vane, respectively. A voltage pulse rising in 10 ns to a maximum flat-top value

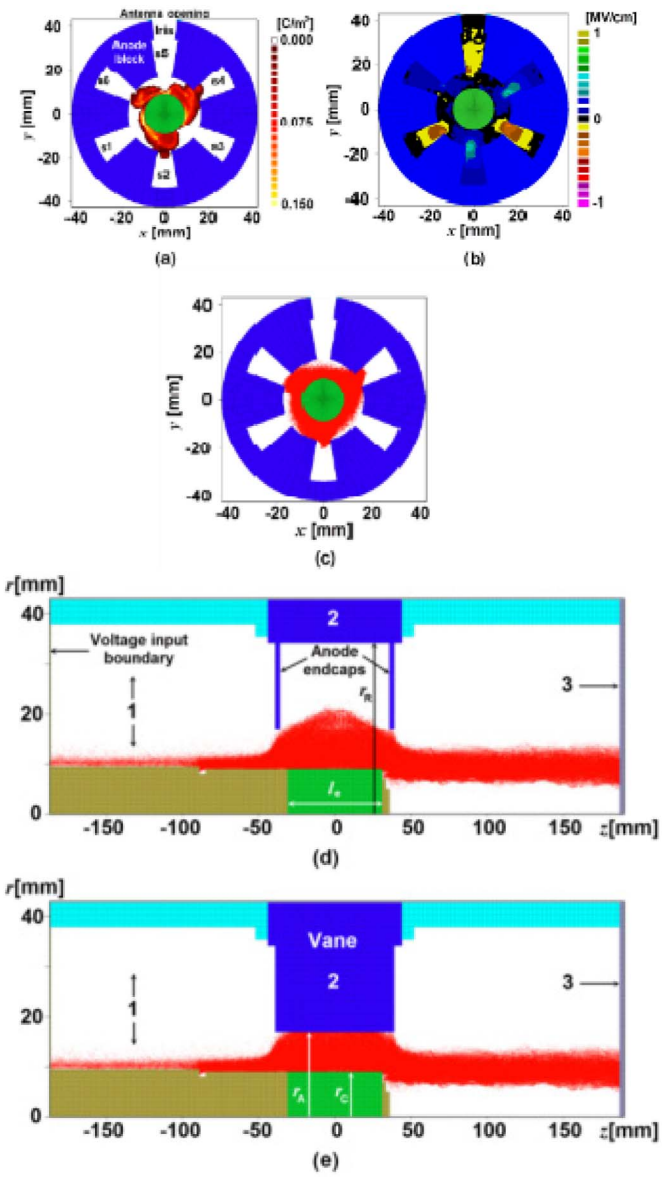


Fig. 1. Geometry of the magnetron model used in the 3-D PIC simulations and some simulation snapshots at $t = 28.8$ ns for $V_{\max} = 190$ kV, $B_{\rm ax} = 0.365$ T, and $l_e = 62$ mm. (a) Contours of the electron charge density distribution, (b) contours of the azimuthal component of electric field, and (c) electron macroparticle positions (red dots) are displayed on an $[x, y]$ cross section perpendicular to $z$ at $z = 0$. Electron positions are drawn on an $[r, z]$ cross section at (d) mid-polar angle crossing slot s2 and (e) mid-polar angle crossing the vane following slot s1 counterclockwise.

of $V_{\max} = 190$ kV is applied along the upstream open boundary at $z = -187$ mm. In all our simulations the cathode radius, the anode radius, and the resonator cavity radius are $r_C = 9$ mm, $r_A = 17$ mm, and $r_R = 34$ mm, respectively. An external axial magnetic field $B_{\rm ax}$ uniform along the entire span of $z$ and constant in time is also applied.

The conducting anode endcaps in Fig. 1(d) cover the ends of the resonator slots s1–s6. We assume that it is possible to limit the electron emission along the cathode to a specific length $l_e$ designated in Fig. 1(d). The electrons flow from the emission region toward the anode block, toward the closed downstream end, and toward the open upstream end [Fig. 1(d) and (e)]. Within the interaction region beneath the anode block, the charge density contour plot seen in Fig. 1(a) has a near-threefold symmetry, which suggests a $\pi$ electromagnetic mode, which is seen in Fig. 1(b) in terms of the azimuthal electric field contours and also in the positions of the electrons in Fig. 1(c). One should though remember that because of the single open radial slot, there is a basic asymmetry in the system, which makes, for most cases studied here, the task of modal analysis difficult, and most cases are not as clear as that seen in Fig. 1(a)–(c). The geometry studied in this paper follows the design of our laboratory magnetron, which will be used in the near future to test the validity of our numerical studies.

The data emerging from a PIC simulation are vast and many quantities are not experimentally observable. In this paper, we calculate the time dependence of the voltage $V$ and the total current $I_T$ flowing in the upstream transmission line at the $z$ position 1 [Fig. 1(d)]. We also calculate the upstream electron flow separately from the displacement current and find that in all cases considered, it is negligibly small. The magnetron anode block and all parts in Fig. 1 drawn in blue and designated by the number 2 collect the electrons flowing toward the anode. This is the magnetron current $I_M$ sometimes called the radial current though it is not, strictly speaking, the result of an electron flow of only radial direction. The axial or leakage current $I_{\rm ax}$ is the result of the electron flow collected on the conducting end of the system designated by 3 in Fig. 1(d). In Fig. 1(a), the opening in slot s5 to a conical antenna through an iris is depicted. The width of the iris is an important parameter but it will not be a variable studied in this paper. The antenna [only its opening seen in Fig. 1(a)–(c)], for all cases was 10-cm long and ends in an absorbing boundary where the radiated microwave power $P_R$ is calculated.

## III. Results of the Numerical Experiments

In Fig. 2, we present the time-dependent values of $V$, $I_T$, $I_M$, and $I_{\rm ax}$ for $r_C = 9$ mm, $l_e = 35$ mm, and $B_{\rm ax} = 0.38$ T.

All time-dependent quantities in Fig. 2 and elsewhere in this paper are mean values calculated by a running average procedure over a 0.34 ns time window, a time interval larger than the period of the fast periodic behavior of the system. In Fig. 3, one can see an example of this process for the radiated power.

In Fig. 3, at first, the mean radiated power is ~50 MW, which then drops, after ~60 ns, to ~25 MW. This pulse-shortening is accompanied by a noticeable voltage drop and total current increase in the time interval 60–70 ns (Fig. 2) which suggests an undermatched impedance situation just as that described in [23] and [24]. Leopold *et al.* [23], [24] have modeled a very similar magnetron but without anode caps (WoAC) covering the axial ends of the resonator cavities. We shall refer to our previous work as WoAC when we compare it with the present system with anode caps (WAC). For the WoAC situation, the axial current becomes negligible soon after the rise-time and the magnetron current is nearly equal to the total current. Here (WAC), the magnetron and

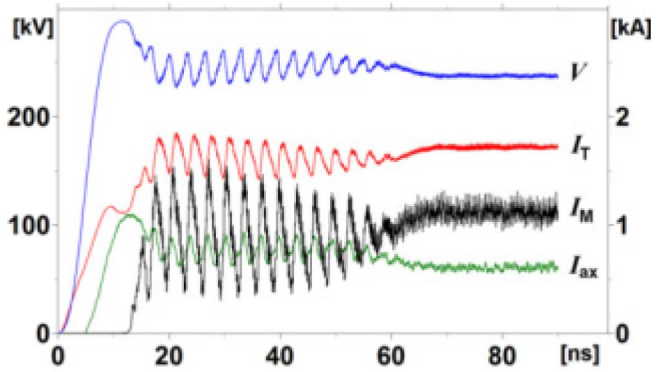


Fig. 2. Time dependence of the mean values of $V$, $I_T$, $I_M$, and $I_{\rm ax}$ for $l_e = 35$ mm and $B_{\rm ax} = 0.38$ T.

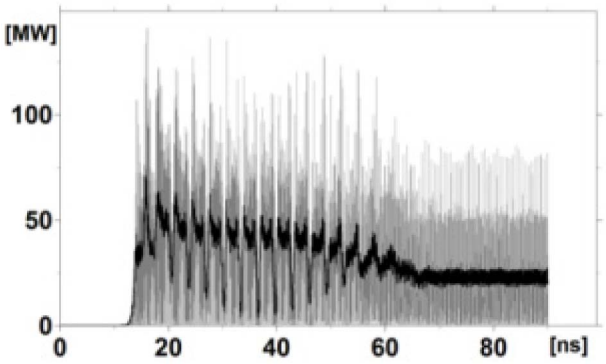


Fig. 3. Instantaneous value of the radiated power (gray) and its mean value (black) calculated by a running average procedure for the parameters set in Fig 2.

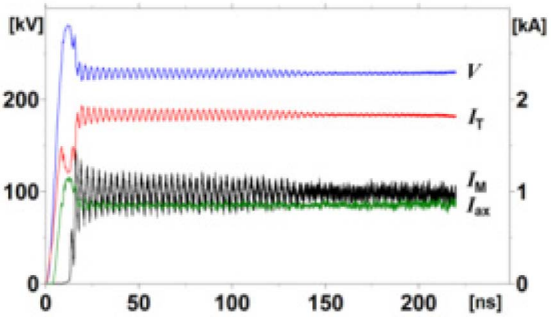


Fig. 4. Same as Fig. 2 but with $l_e = 62$ mm.

axial currents are of the same order of magnitude up to power pulse-shortening when the magnetron current increases and the axial current slightly decreases. Note that since the upstream electron flow is negligible, $I_T \cong I_M + I_{\rm ax}$.

In Fig. 4, the electron emission length is increased to $l_e = 62$ mm. This, apart from the now dampened underlying slow oscillatory behavior, leaves the level of all measured quantities unchanged in time.

The average values of the axial and magnetron currents remain of the same order of magnitude, indicating that the axial current is a drain for the excess magnetron current. This keeps the magnetron impedance sufficiently high for alleviating pulse-shortening. Fig. 5 shows the result of the running average of the microwave power in comparison with the

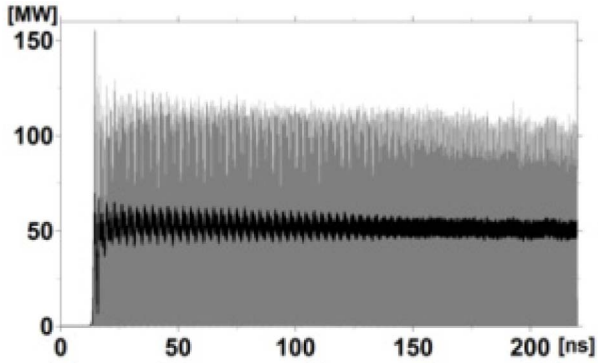


Fig. 5. Same as Fig. 3 for the conditions set in Fig. 4.

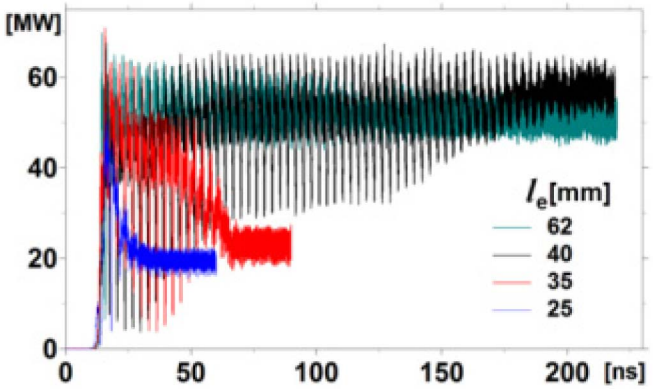


Fig. 6. Time dependence of the mean radiated power $P_R$ for various values of $l_e$ and fixed $B_{\rm ax} = 0.38$ T.

instantaneous behavior with no evidence of pulse-shortening up to very long times.

As $l_e$ is increased above 40 mm, pulse-shortening disappears and the slow oscillations dampen. This is reflected in the time dependence of the mean radiated power shown in Fig. 6 for various values of $l_e$.

For $l_e \leq 35$ mm, pulse-shortening causes a drop in the radiated power to the level of ~20 MW. For $l_e \geq 40$ mm, the radiated power efficiency increases from ~5% to ~15%. Note that the averaging process leaves a considerable slow oscillatory behavior (period ~3 ns), which disappears with pulse-shortening, survives over a long period of time for $l_e \geq 40$ mm, but dampens for the largest $l_e$ considered.

Let us discuss the magnetron operation in terms of impedance matching. In Fig. 7(a), the time dependence of the mean values of the total impedance $Z_T = V/I_T$, the magnetron impedance $Z_M = V/I_M$, and the axial load impedance $Z_{\rm ax} = V/I_{\rm ax}$ for $l_e = 35$ mm are displayed. In the 50–70 ns time interval, power pulse-shortening (Fig. 2) is accompanied by a dynamical impedance change. The decrease in the voltage, the corresponding decrease in $I_{\rm ax}$, and increase in $I_M$ and $I_T$ seen in Fig. 2 result in a decrease in $Z_T$ and $Z_M$ and an increase in $Z_{\rm ax}$. For the increased value of $l_e$ in Fig. 7(b), the values of $Z_T$, $Z_M$, and $Z_{\rm ax}$ remain almost constant.

We have tested and confirmed for all WAC cases considered that $Z_T \cong Z_M \times Z_{\rm ax}/(Z_M + Z_{\rm ax})$, that is, the magnetron and the axial load act as two loads connected in parallel to

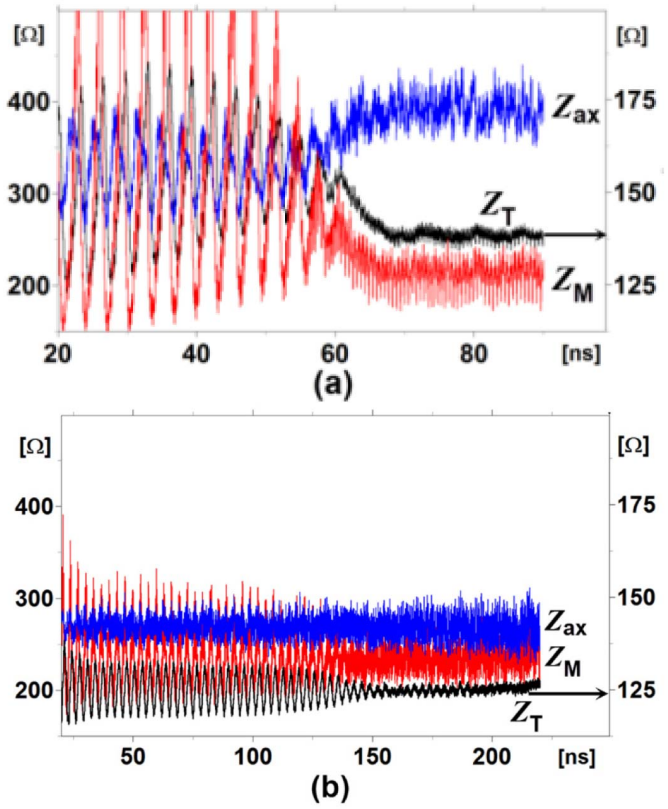


Fig. 7. Time dependence of the mean values of $Z_T$ (black), $Z_M$ (red), and $Z_{\text{ax}}$ (blue) for (a) $l_e = 35$ mm and (b) 62 mm.

the upstream transmission line leading to the power generator. It should be noted that the matched value of $Z_T$ is about the same [$\sim$125 $\Omega$, Fig. 7(b)] as for the WoAC case [23]. As mentioned in [23], the vacuum impedance of the transmission line, through which the excitation signal is introduced in the simulations, is lower than the matched value of $Z_T$ because of the magnetically insulated return current to the cathode.

For the WoAC case, $Z_{\text{ax}}$ is very large so for the impedances to match, $Z_T \cong Z_M$. When for a given voltage the magnetron current became too high to be sustainable, the voltage decreased and the current increased accompanied by a power drop. Because of this, we were able to eliminate pulse-shortening for the WoAC magnetron by reducing the emitted current.

Though an undermatched impedance is responsible for power pulse-shortening for the WAC too, in contrast to the WoAC, pulse-shortening is eliminated by increasing the emitted current with increased emission length $l_e$. This increases the total current $I_T$ but allows more current to flow as axial current $I_{\text{ax}}$, which does not allow $Z_{\text{ax}}$ to increase and consequently $Z_M$ to decrease. We explain the electrodynamics of this process in Section V.

In a magnetron, the electromagnetic wave gains energy from the drifting electron beam, in particular from electrons at the surface of the Brillouin flow. Radiated energy is gained when the electric field in a magnetron cavity is decelerating electrons. These electrons then drift toward the anode while losing their potential energy to the traveling wave. The balance between the electron flow in phase with the azimuthal

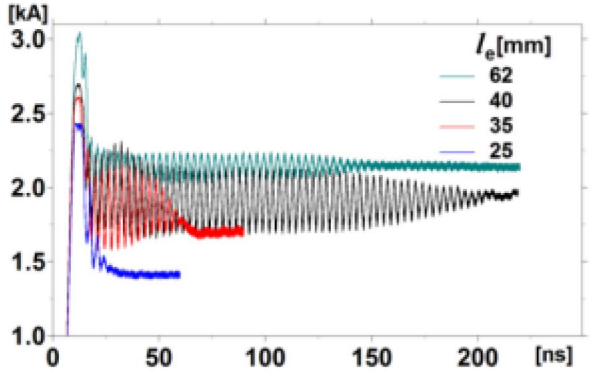


Fig. 8. Time dependence of the mean value of $I_d$ averaged over its values in the six cavities for various values of $l_e$ and fixed $B_{\text{ax}} = 0.38$ T.

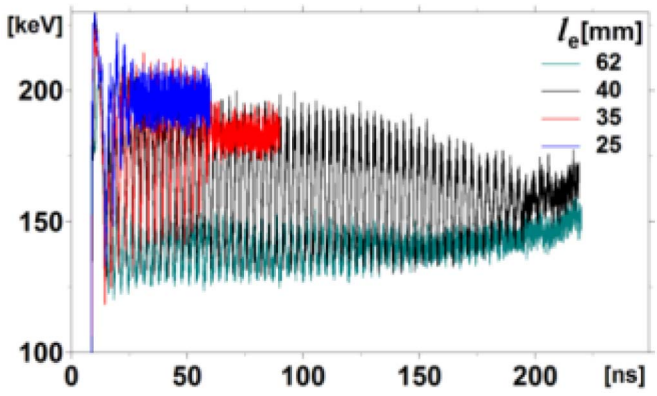


Fig. 9. Time dependence of the mean kinetic energy of the electrons $E_K$ collected on the anode surfaces for various values of $l_e$ and fixed $B_{\text{ax}} = 0.38$ T.

microwave electric field and that out of phase determines the radiation efficiency of the magnetron. We have seen (Fig. 2) that power pulse-shortening is accompanied by an increase in the magnetron current. We have discussed this seemingly counterintuitive observation for the WoAC case by calculating the azimuthal drift current. The azimuthal drift current $I_d$ is defined as the current crossing the $[r, z]$ surface at the mid polar angle of a cavity and indicates the maximum available drift current that could transfer its energy into radiation. In Fig. 8, we present the time dependence of $I_d$ for different values of $l_e$. The mean value of $I_d$ is first calculated in each of the six cavities and then the average of these six values is taken as a function of time. This is needed for clarity, because the azimuthal drift current varies somewhat between cavities due to the built-in polar asymmetry of our magnetron.

For $l_e = 35$ mm, with power pulse-shortening $I_T$ and $I_M$ increase (Fig. 2), but $I_d$ decreases (Fig. 8). This decrease accompanies the drop in the radiated power as was the case for the WoAC [23]. When there is no power pulse-shortening, $I_d$ stays at the same high level. For the intermediate metastable case $l_e = 40$ mm, $I_d$ oscillates together with all other calculated quantities until, after a very long time, it settles at a fixed value.

In Fig. 9, the time dependence of the mean kinetic energy of electrons collected on the anode surfaces $E_K$ is depicted for various values of $l_e$.

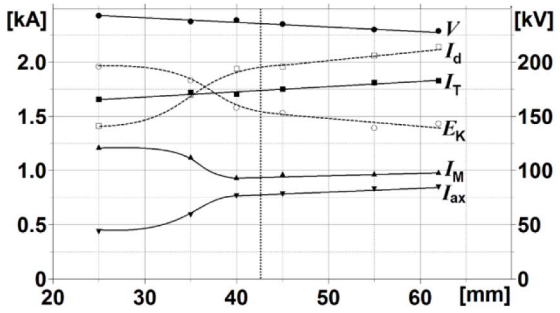


Fig. 10. Steady-state mean values of $V$, $I_T$, $I_M$, $I_{\rm ax}$, $I_d$, and $E_K$ as functions of the emission length $l_e$ for fixed $B_{\rm ax} = 0.38$ T. These values are averaged over the large period oscillation when these occur. The dotted vertical line denotes the value of $l_e$ below which pulse-shortening exists.

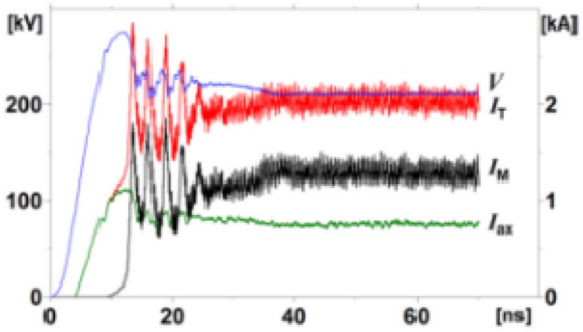


Fig. 11. Same as Fig. 2 for $l_e = 62$ mm and $B_{\rm ax} = 0.36$ T.

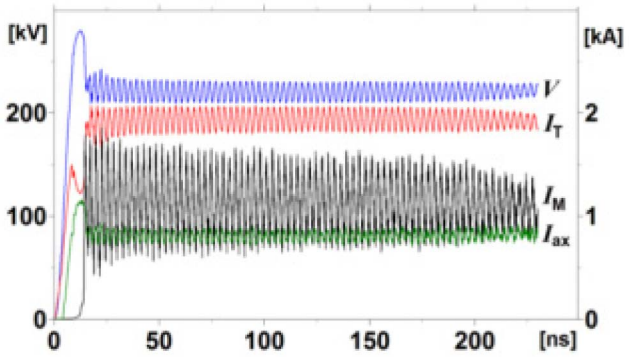


Fig. 12. Same as Fig. 2 for $l_e = 62$ mm and $B_{\rm ax} = 0.365$ T.

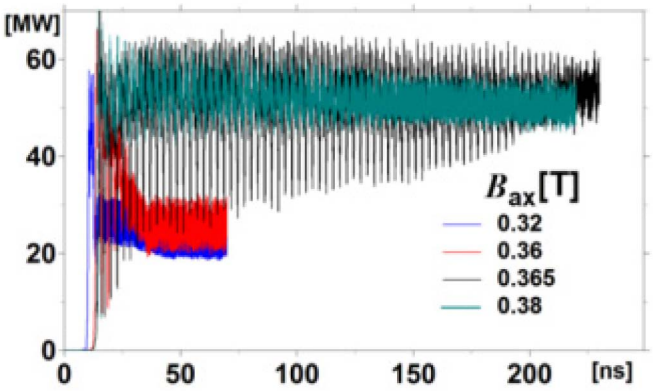


Fig. 13. Time dependence of the mean radiated power $P_R$ for $l_e = 62$ mm and various values of the applied fixed axial magnetic field $B_{\rm ax}$.

In Fig. 9 for $l_e < 40$ mm, the mean kinetic energy is close to the value of the energy of particles accelerated by the anode–cathode voltage gap. This indicates that the number of drifting electrons, which transfer their energy to the electromagnetic field, is small, which explains the low power of the radiated field. For $l_e = 62$ mm, there is a dramatic drop in the mean kinetic energy consistent with the increase in the radiated power. For $l_e = 40$ mm, the mean electron kinetic energy slowly oscillates between these two limits until it settles, a pattern followed by the radiated power too (Fig. 6).

For all cases discussed, a significant large period (~3 ns) oscillatory behavior exists, which dampens as pulse-shortening is eliminated. We shall discuss this in Section IV.

We have so far experimented with the emission length parameter for fixed axial magnetic field and applied voltage. In Fig. 10, we summarize the steady-state results for this parameter change. As $l_e$ is increased, the total current increases while the voltage decreases. At the same time, this causes the magnetron current to decrease and the axial current to increase until the impedances match. As pulse-shortening disappears at $l_e > 40$ mm, the steady-state mean value of $E_K$ strongly decreases whereas $I_d$ increases. The latter becomes higher than the value of $I_T$ and exceeds more than twice the current collected on the anode.

We test next the effect of varying the applied axial magnetic field. In Fig. 11, we draw the time-dependent values of $V$, $I_T$, $I_M$, and $I_{\rm ax}$ for $l_e = 62$ mm. We have reduced the axial magnetic field from 0.38 T (Fig. 4) to 0.36 T (Fig. 11).

At $B_{\rm ax} = 0.36$ T in Fig. 11 in the interval 30–40 ns, the voltage decreases and the total current increases indicating an undermatched impedance situation accompanied by power pulse-shortening, which is seen in Fig. 13. At the same time and just as seen before, $I_M$ increases and $I_{\rm ax}$ decreases. A small increase in the axial magnetic field to 0.365 T eliminates pulse-shortening (Fig. 13) while $V$, $I_T$, $I_M$, and $I_{\rm ax}$ remain at the same level in time (Fig. 12).

The time dependence of the dynamic impedances $Z_M$, $Z_{\rm ax}$, and $Z_T$ for the last two cases (Figs. 11 and 12) is very similar to that seen in Fig. 7. In the time interval where the power pulse shortens, $Z_T$ and $Z_M$ decrease while $Z_{\rm ax}$ increases. As $B_{\rm ax}$ is increased and power pulse-shortening is eliminated, the three impedances keep on average level.

The time dependence of the mean radiated power for various magnetic field strengths and fixed $l_e$ is seen in Fig. 13 (compare to Fig. 6 where $l_e$ is varied for fixed Bax). The mean radiated power pulse shortens for $B_{\rm ax} \leq 0.36$ T after a few strong slow oscillations. It is sufficient to increase the axial magnetic field from 0.36 to 0.365 T for pulse-shortening to disappear but the strong slow (~3 ns period) oscillatory behavior between ~30 and ~60 MW keeps on over a long period of time until it dampens. For higher magnetic fields, $B_{\rm ax} = 0.38$ T, these oscillations are much weaker and the high radiated power is sustained over time. At $B_{\rm ax} = 0.4$ T (not presented in Fig. 13) the slow oscillations

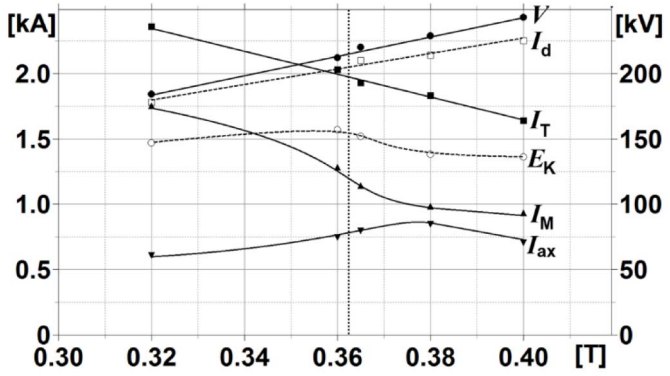


Fig. 14. Steady-state mean values of $V$, $I_T$, $I_M$, $I_{\rm ax}$, $I_d$, and $E_K$ as functions of the axial magnetic field, $B_{\rm ax}$ for fixed $l_e = 62$ mm. These values are averaged over the large period oscillation when these occur. The dotted vertical line denotes the value of $B_{\rm ax}$ below which pulse-shortening exists.

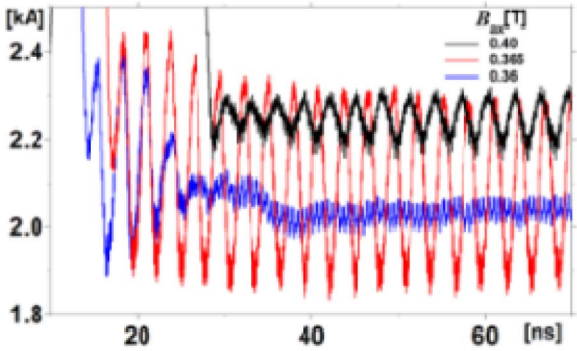


Fig. 15. Time dependence of the mean value of $I_d$ averaged over its value in the six cavities for $l_e = 62$ mm and various values of $B_{\rm ax}$.

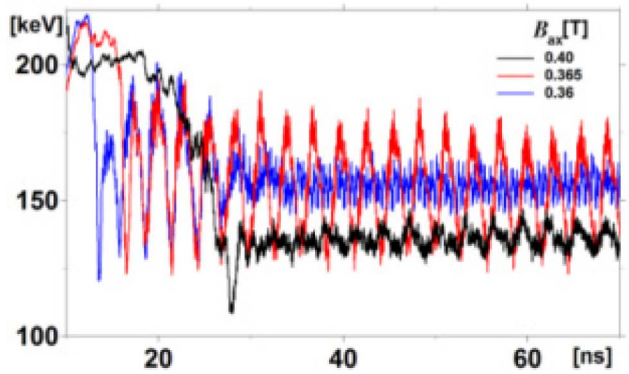


Fig. 16. Time dependence of the mean kinetic energy of the electrons collected on the anode surfaces for $l_e = 62$ mm and various values of $B_{\rm ax}$.

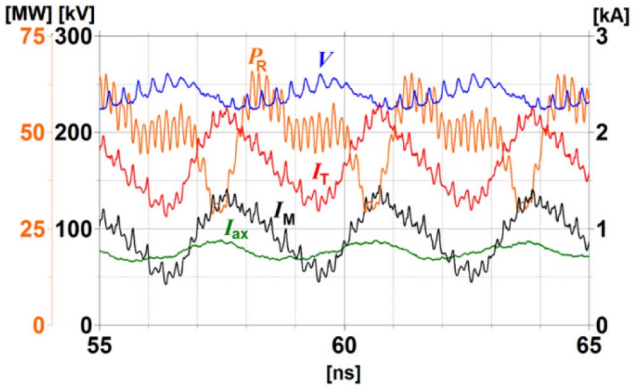


Fig. 17. Time dependence of the mean values of $V$, $I_T$, $I_M$, $I_{\rm ax}$, and $P_R$ for $l_e = 40$ mm and $B_{\rm ax} = 0.38$ T.

dampen further but the power starts to decrease (∼45 MW) consistent with the approach of the Buneman–Hartree (BH) cutoff limit. It is interesting to note that there seems to be an unstable region between the Hull limit of the magnetic field for magnetic insulation and the BH cutoff where magnetic insulation becomes too strong. It is difficult to estimate the magnetic field at the BH limit for these conditions by analytic means because the characteristic mode of the system does not clearly resolve (see Section IV).

Fig. 14 summarizes the mean steady-state values of the voltage and the different values of the various currents for fixed $l_e = 62$ mm and various values of $B_{\rm ax}$. In contrast to Fig. 10, as the axial magnetic field is increased and pulse-shortening disappears for $B_{\rm ax} > 0.36$ T, at steady state the total current decreases as more electrons are magnetically insulated from the anode. Consequently, the voltage increases. On the other hand, as in Fig. 10, impedance matching is approached by decrease in the magnetron and increase in the axial current. As the applied magnetic field is increased close to the BH limit (∼0.4 T), the radiated power decreases (Fig. 13) and both magnetron and axial currents decrease (Fig. 14).

Even though the magnetron current decreases with increasing $B_{\rm ax}$, the mean azimuthal drift current increases (Fig. 15). At the same time, the voltage increases (Fig. 14) but the mean kinetic energy of the electrons collected on the anode decreases (Fig. 16). This behavior is very similar to that seen when $l_e$ is increased for fixed $B_{\rm ax}$ (Figs. 8 and 9) except that for the latter the total current increases (Fig. 10). These observations suggest that an increased proportion of lower energy azimuthally drifting electrons is responsible for increased radiated power and the increase or decrease in the total current or the decrease in the magnetron current is not directly indicative of higher energy transfer. Steady-state mean values of $I_d$ and $E_K$ for various values of $B_{\rm ax}$ are displayed in Fig. 10.

The numerical experiments presented in this section show that the WAC magnetron differs from the WoAC magnetron because of the considerable role played by the axial current. Eliminating pulse-shortening requires for the WAC the increase in the axial current. We have demonstrated this by two parameter changes: increasing $l_e$ for fixed $B_{\rm ax}$ or increasing $B_{\rm ax}$ for fixed $l_e$. Between the parameter regions where pulse-shortening exists and where it does not, there is a transition region where the mean radiated power contains a slow periodic pattern, which we discuss next.

## IV. Transition Region

In Fig. 17, the behaviors of the mean values of $V$, $I_T$, $I_M$, $I_{\rm ax}$, and $P_R$ within a small time-interval are displayed for the parameters in the transition regions found in Section III.

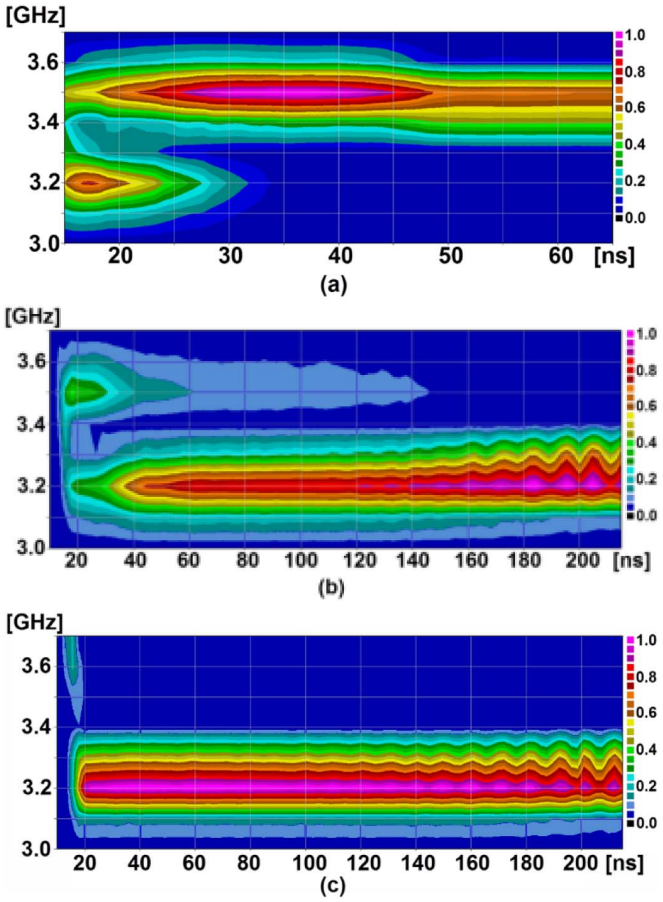


Fig. 18. Time-frequency contour plots of the azimuthal electric field near the antenna boundary for $B_{\mathrm{ax}} = 0.38$ T. (a) $l_e = 25$ mm. (b) $l_e = 40$ mm. (c) $l_e = 62$ mm. The amplitudes of the contours in all frames are normalized to 1. The frequency region drawn contains the highest amplitude frequency components of the fast Fourier transform.

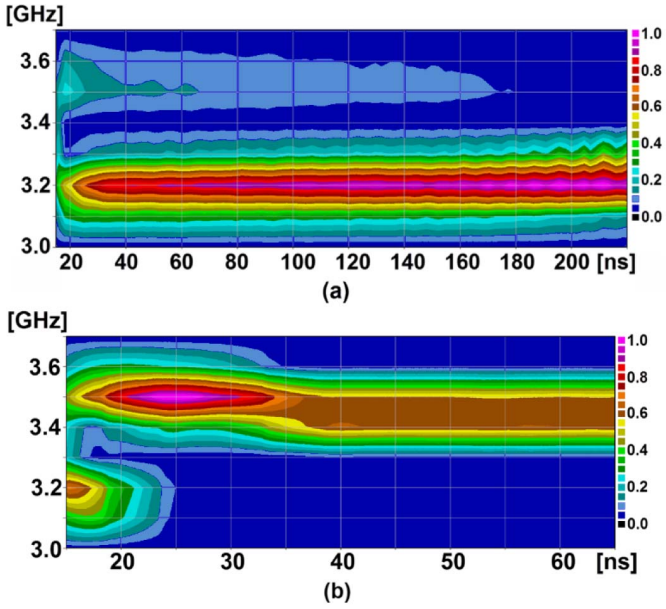


Fig. 19. Same as Fig. 18 for (a) $B_{\mathrm{ax}} = 0.365$ T and (b) 0.36 T ($l_e = 62$ mm).

The structure of the slow periodic behavior seen in Fig. 17 reflects the balance which needs to be preserved during this oscillating power flow. During half of each such period while the total current increases the voltage decreases and the radiated power decreases. The increase in the magnetron current contributes most of the increase in the total current. Though the axial current increases too, but not significantly, it keeps its value high. During the following half period the radiated power increases, the currents decrease and the voltage increases. The same trends seen in Fig. 17 are observed for all the cases with slow large amplitude oscillatory behavior. A small change near $l_e = 40$ mm at $B_{\mathrm{ax}} = 0.38$ T (Fig. 17) or a small change near $B_{\mathrm{ax}} = 0.365$ T at $l_e = 62$ mm (Fig. 12) can shift the behavior strongly toward pulse-shortening on the one hand and stable high power RF radiation on the other hand (Figs. 6 and 13).

Next we analyze the time–frequency behavior of the azymuthal electric field near the boundary of the conical antenna. Time-frequency contour plots for various values of $l_e$ and fixed $B_{\mathrm{ax}} = 0.38$ T are drawn in Fig. 18. For $l_e = 62$ mm the transition region [Fig. 19(a)] is seen between 0.38 T [Fig. 18(c)] and $B_{\mathrm{ax}} = 0.36$ T [Fig. 19(b)].

The decrease in the amplitude of the contours corresponding to 3.5 GHz with time in Figs. 18(b) and 19(b) corresponds to the damping of the amplitudes of the slow oscillations in RF power seen in Figs. 6 and 13, respectively.

It seems that for the parameter space $l_e$ and $B_{\mathrm{ax}}$ considered, there are regions where two frequencies compete and the mean radiated power amplitude oscillates slowly ($\sim$3 ns period) between a low and a high value. This region of mode competition is the boundary between the parameter region where pulse-shortening occurs and the region where it is eliminated by impedance matching.

To ascertain this explanation, we tested the transition region by increasing the distance to the downstream endplate (3 in Fig. 1), the distance of the voltage input port from $z = 0$, or the length of the conical antenna each by 1 m, respectively. None of these changes influenced the behavior of the magnetron, which means that the internal time dependences are not the result of delays of electromagnetic scattering from these boundaries. It is very difficult to analyze the electromagnetic modes developing in such a magnetron because of the perturbing asymmetry introduced by the single radial open slot. We have seen in Fig. 1(a)–(c) that a $\pi$-like mode seems to develop but this is not the only existing mode. The characteristic frequencies of the two modes are 3.2 and 3.5 GHz (Figs. 18 and 19).

Mode competition in relativistic magnetrons is not a new concept [6]. Early 2-D PIC calculations [20], [27] have also identified the cause of the long-period beating structures such as those seen in Figs. 6, 13, and 17 as the result of mode competition.

One could deduce from the results in Figs. 18(b) and 19(a) that mode competition is the cause of pulse-shortening. On the other hand, as we change parameters to match impedances, mode competition is eliminated too [Fig. 18(c)]. We have not found a direct connection between the parameter changes and the modes developing in the magnetrons.

We have seen in this section that in the transition region, large low-frequency power beats appear, which are due to

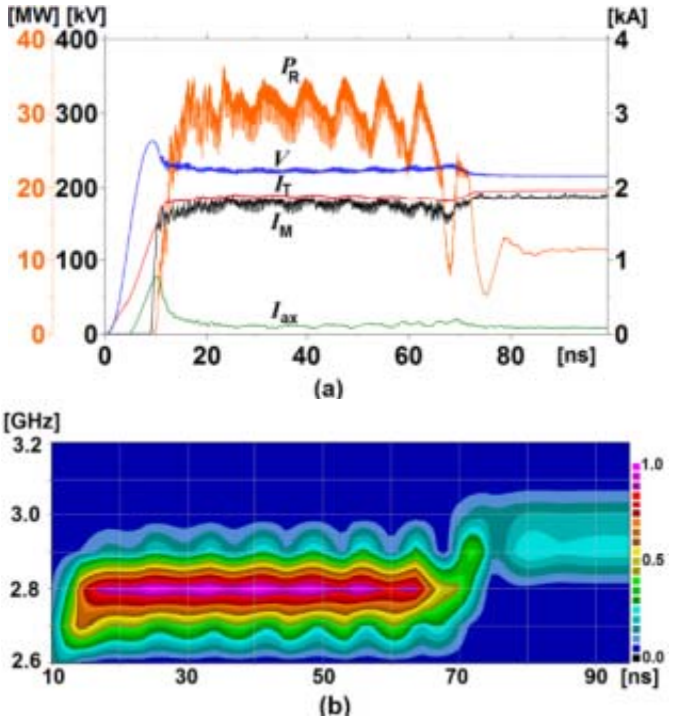


Fig. 20. (a) Time dependence of the mean values of $V$, $I_T$, $I_M$, $I_{\rm ax}$, and $P_R$ for a WoAC magnetron with $l_e = 18$ mm, $r_C = 6.25$ mm, $B_{\rm ax} = 0.27$ T, and an input voltage of 190 kV. (b) Time–frequency contour plots of the azimuthal electric field near the antenna boundary.

mode competition. By varying $l_e$ for fixed $B_{\rm ax}$ or varying $B_{\rm ax}$ for fixed $l_e$ by a small amount, the mean power remains either large with decreasing beats or becomes low after pulse-shortening.

## V. Electrodynamical Observations

So far, we have studied the WAC and the WoAC [23], [24] magnetrons by analyzing the electronic observables such as voltages, currents, and impedances. Indeed, we find for both magnetron types that undermatched magnetron impedance relative to the input impedance representing a real pulsed voltage generator is responsible for radiated power pulse-shortening. We also pointed out the different behavior of the axial current in these two magnetron types, which has an important effect on the way impedance matching is achieved. In this section, we study the development of the various electromagnetic observables in both cases in an attempt to understand how their behavior relates to the electronic observables.

The comparison between our WAC and WoAC magnetrons has to be considered very carefully because these do not differ only in the presence or lack of anode caps. The cathode radius considered for the WoAC is ∼6 mm compared with 9 mm for the WAC. The applied magnetic field was ∼0.27 T for the WoAC and 0.32–0.40 T for the WAC. These are different parameter regions for which we found that impedance matching eliminates pulse-shortening.

Leopold *et al.* [23] have shown that by reducing the emission length $l_e$ of the WoAC ($r_C = 6.25$ mm but otherwise the same geometrical parameters as the above WAC) from 21.6 to 14.4 mm, pulse-shortening was alleviated. In Fig. 20(a), we present results for the WoAC magnetron for $l_e = 18$ mm, $r_C = 6.25$ mm, $B_{\rm ax} = 0.27$ T, and an input voltage of 190 kV. For this value of the emission length, pulse-shortening occurs in the 60–80 ns time interval. Note the drop in the axial current occurring soon after the voltage rise-time in contrast to the WAC.

In Fig. 20(b) time-frequency contours are drawn. The mode centered at the lower frequency 2.8 GHz is stable up to ∼65 ns when it is taken over by the second mode at 2.9 GHz after a few strong power beats. The characteristic frequencies of the two modes are close and their widths overlap in the ∼15–65 ns interval resulting in a much longer beating period (∼10 ns) than that seen for the WAC. The change in the acting mode corresponds to the time when the voltage decreases and the current increases. For the WAC, the characteristic frequencies of the two modes are further apart and do not overlap [Figs. 18(b) and 19(a)] resulting in a much shorter beating period.

In Fig. 21, we present contours of the field components $E_r$, $E_\theta$, $E_z$, and $B_\theta$ and contours of the absolute value of the electron space charge density $|Q_e|$ for the WoAC of Fig. 20 and for the WAC of Figs. 2 and 3. Fig. 21 depicts the behavior of these electromagnetic observables along the $[z, r]$ cross section at the mid polar angle of cavity S1.

The contours in Fig. 21 are obtained at points in time after the applied voltage has fully risen, the interaction of the emitted electrons with the magnetron cavities is fully developed, and the radiated power has reached its maximum. Before the rise time of the radiated power, the azimuthal component of the electric field $E_\theta$ is negligibly small, while the axial component $E_z$ is very similar to that shown in Fig. 21(c) and (h). The value of $E_z$ at the edge of the emission region and the tip of the cathode is sufficient to move electrons rotating azimuthally around the cathode downstream. With the axial current, $B_\theta$ develops which by $E_r \times B_\theta$ ascertains the charge density flow in the axial direction. However, when the radiated power has reached its maximum, for the WoAC case, the axial electron flow drops to negligible values [Fig. 21(e)], whereas in the WAC case, it continues undisturbed [Fig. 21(j)]. The reason for this is the different spatial distribution of the fully developed $E_\theta$ relative to the emission region [compare Fig. 21(b) with Fig. 21(g)].

For the WoAC, $E_\theta$ [Fig. 21(b)] is of the same order of magnitude as $E_r$ [Fig. 21(a)] and it spreads in $z$ a long way from the edges of the emission region. The magnitude and axial spread of $E_\theta$ ensures that electrons, which run away axially due to $E_r \times B_\theta$, are moved away from the axis in the radial direction by $E_\theta \times B_{\rm ax}$. Indeed, one can see that for the WoAC the contours of $E_r$ and $B_\theta$ do not spread into the downstream cavity, indicating that there is no axial current there [compare Fig. 21(a) with Fig. 21(f) and (d) with Fig. 21(i)].

In Fig. 22(a), the mean absolute value of $E_\theta$ is drawn along $z$ at $r = r_A$ at the mid polar angle of cavity S1 for the WoAC and WAC. For the WAC magnetron, $E_\theta$ is bound by the anode caps [Fig. 21(g)]. At the inside boundaries of the anode caps located at $z = \pm 36$ mm, $E_\theta \to 0$ for the WAC. $E_\theta$ is significantly larger at these locations for the WoAC and spreads even further in $z$.

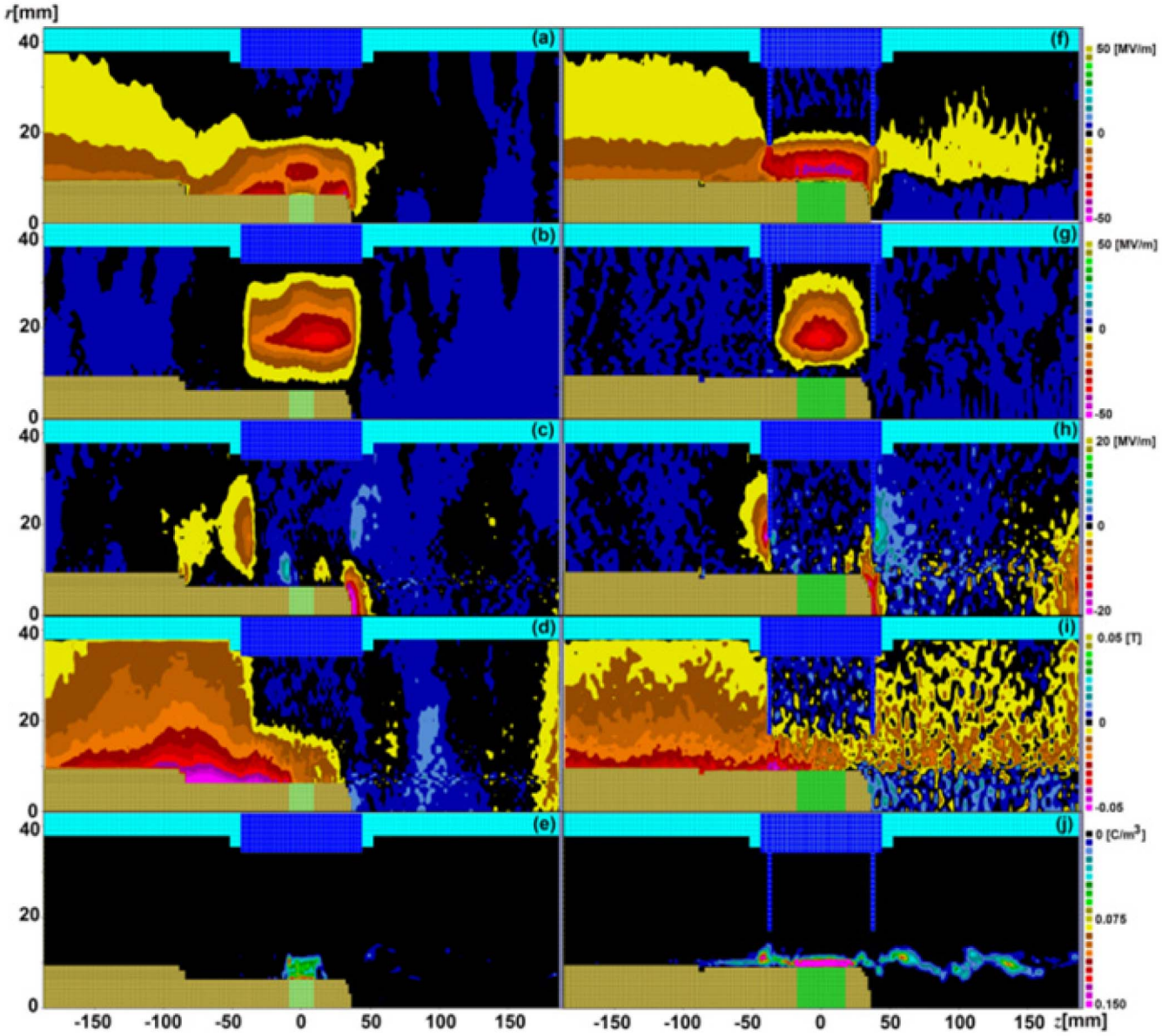


Fig. 21. Contours along the [$z$, $r$] cross section at the mid polar angle of cavity S1 of the field components (a) $E_r$, (b) $E_\theta$, (c) $E_z$, and (d) $B_\theta$ and of (e) $|Q_e|$ for the WoAC of Fig. 20 at $t = 15$ ns. (f)–(j) Same quantities for the WAC of Figs. 2 and 3 at $t = 17.1$ ns, respectively.

In Fig. 22(b), $E_\theta$ is drawn along $r$ at various fixed values of $z$. Note that $l_e$ for the WAC is between $z = \pm 17.5$ mm, whereas for the WoAC, it is between $z = \pm 9$ mm. For the WAC, $E_\theta$ is negligibly small for $r < 12$ mm for all values of $z$. For the WoAC, $E_\theta$ is present close to the cathode and along $z$ beyond the edges of the magnetron anode block. This leaves for the WAC, in contrast to the WoAC case, a region between the emission area's downstream edge, the cathode edge, and the downstream anode cap where $E_\theta \sim 0$. Electrons reaching this region will no longer be moved away radially by $E_\theta \times B_{\mathrm{ax}}$ and will flow axially. (Below we shall refer to this as the *runaway* region.)

The contours in Fig. 21(f) and (i) of $E_r$ and $B_\theta$, respectively, are spread in the downstream cavity indicating the existence of the axial current in contrast to Fig. 21(a) and (d). The strong presence of $E_r \times B_\theta$ and $E_z$ [Fig. 21(c) and (h)] in the *runaway* region, together with the absence of $E_\theta$, explains the persistence in time of the axial current in the WAC magnetron.

As $l_e$ is increased and the edge of the emission region gets closer to the position of the anode endcaps in a WAC, both $E_z$ and $B_\theta$ increase in the *runaway* region, so that more current is drained axially, which explains the decrease in the magnetron current and impedance matching.

The above behavior is similar in all cavities apart from $E_\theta$, which is affected by the azimuthal rotation of the electron space charge cloud around the cathode. Because of the azimuthal asymmetry and mode competition, the values presented in Fig. 22 are not the same in every cavity as seen in Fig. 23.

Even though the averaging process over time should result in a fixed field pattern, because of mode competition the structure seen in Fig. 23 rotates in time apart from the asymmetric

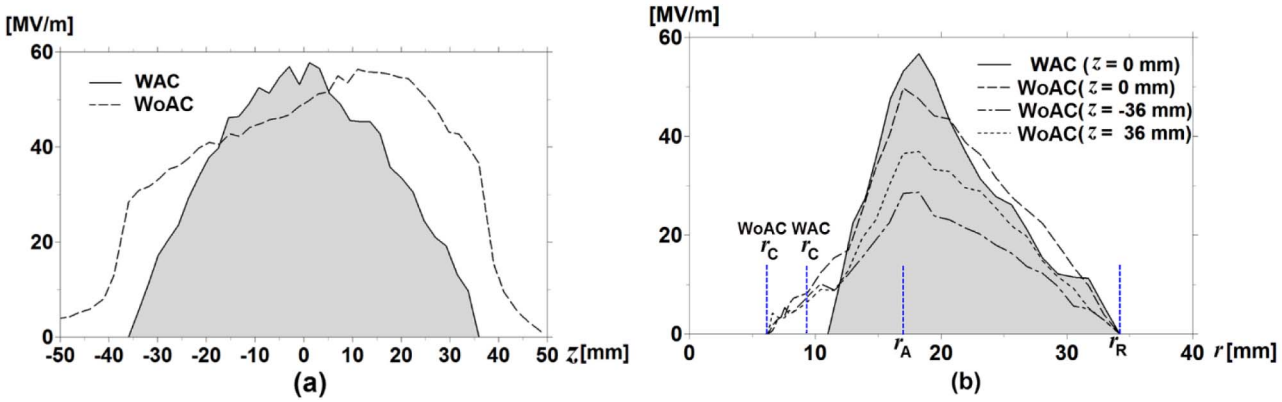


Fig. 22. Mean absolute value of $E_\theta$ in cavity S1 for the WoAC [$t = 15$ ns, Fig. 21(b)] and the WAC [$t = 17.1$ ns, Fig. 21(g)] (a) versus $z$ at $r = r_A$ and (b) versus $r$ at various $z$ positions.

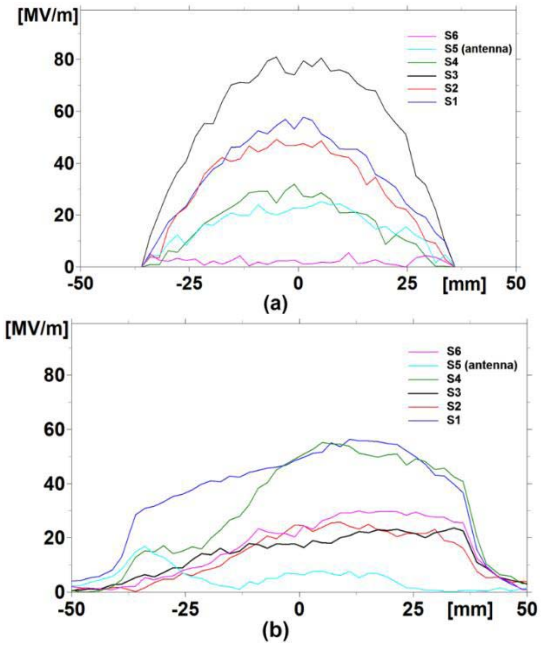


Fig. 23. Mean absolute value of $E_\theta$ for (a) WAC ($t = 17.1$ ns) and (b) WoAC ($t = 15$ ns) versus $z$ at $r = r_A$ in each cavity.

behavior in the open cavity. Nevertheless, the effect of the endcaps bounding $E_\theta$ in a WAC magnetron, and in particular at the downstream end, is seen in all cavities. This supports our explanation regarding the presence of the axial current in a WoAC magnetron.

We have followed the electrodynamical observables (Fig. 21) in time in an attempt to understand the changes in the electronic observables during the pulse-shortening process, namely, the rise of the magnetron current and the energy of the electrons collected on the anode, for both the WoAC and the WAC magnetrons studied. The picture becomes extremely complicated because of the asymmetry and the mode competition, which as described in Section IV and above is different for the WAC and the WoAC. There are distinct changes observed in both the distribution of the electron space charge and that of $E_\theta$ but very difficult to characterize. One can assume that an important role in the pulse-shortening process belongs to the azimuthal electric field component produced by the space charge of the electron spokes, which is to be distinguished from the radiative field.

We have demonstrated that the presence or absence of anode caps has a strong effect on the electrodynamic development of these systems. The behavior of the various electromagnetic field components explains the presence of the axial current in a WAC and its absence in a WoAC magnetron. We were unable at this point to relate the changes in the electronic observables to electromagnetic observables during the pulse-shortening process. These will be looked at carefully in our future work.

## VI. Conclusion

The numerical experiments presented in this paper show that a WAC and a WoAC six-vane single radial output magnetron differ in their behavior. Even without being able to characterize exactly the operating modes, these are different for the two systems and at different frequencies. Thus, the two systems have different resonant behaviors.

For both systems, we have demonstrated that impedance matching between the magnetron load and the power generator is an important factor and the ways suggested to improve matching do indeed stabilize the systems at higher radiating power.

We have seen that the main difference between the WAC and the WoAC magnetrons is in the behavior of the axial current, which affects the way impedance matching can be achieved. We have been able to explain this difference by analyzing the electrodynamic behavior of the two systems.

We assumed so far that the width of the emission region $l_e$ can be controlled, which may be difficult to achieve experimentally. Because of this, the WAC is probably more appropriate for experimental study because for fixed axial magnetic field, $l_e$ needs to be increased to improve impedance matching.

Experimental voltage pulse shapes have probably a strong effect on the behavior of these systems. Keeping the impedances matched for a particular power-generator voltage time-profile needs to be considered separately for each system. Nonetheless, our work suggests that impedance matching

between the power generator and the magnetron load can avoid pulse-shortening provided that plasma does not expand and short the space between the cathode and the anode.

In this paper, we have varied only the emission length and the magnetic field for fixed cathode, anode, and cavity radii. Changing these radii, apart from affecting the operation range of the magnetron (the Hull and BH magnetic field limits), will influence the values of the emission length required for impedance matching and the elimination of pulse-shortening. It is understood that different geometrical parameters can change the behavior of a specific magnetron operation, and the electrodynamical understanding presented in our work suggests ways to resolve the problem of pulse-shortening when plasma does not play a role.

## REFERENCES


[1] G. Bekefi and T. J. Orzechowski, "Giant microwave bursts emitted from a field-emission, relativistic-electron-beam magnetron," *Phys. Rev. Lett.*, vol. 37, no. 6, pp. 379–382, Aug. 1976.

[2] A. Palevsky, G. Bekefi, and A. T. Drobot, "Numerical simulation of oscillating magnetrons," *J. Appl. Phys.*, vol. 52, no. 8, pp. 4938–4941, Aug. 1981.

[3] H.-W. Chan, C. Chen, and R. C. Davidson, "Computer simulation of relativistic multiresonator cylindrical magnetrons," *Appl. Phys. Lett.*, vol. 57, no. 12, pp. 1271–1273, Sep. 1990.

[4] R. C. Davidson, H.-W. Chan, C. Chen, and S. Lund, "Equilibrium and stability properties of intense non-neutral electron flow," *Rev. Mod. Phys.*, vol. 63, no. 2, pp. 341–374, Apr. 1991.

[5] R. W. Lemke, T. C. Genoni, and T. A. Spencer, "Three-dimensional particle-in-cell simulation study of a relativistic magnetron," *Phys. Plasmas*, vol. 6, no. 2, pp. 603–613, Feb. 1999.

[6] R. W. Lemke, T. C. Genoni, and T. A. Spencer, "Effects that limit efficiency in relativistic magnetrons," *IEEE Trans. Plasma Sci.*, vol. 28, no. 3, pp. 887–897, Jun. 2000.

[7] Y. M. Saveliev, S. N. Spark, B. A. Kerr, M. I. Harbour, S. C. Douglas, and W. Sibbett, "Effect of cathode end caps and a cathode emissive surface on relativistic magnetron operation," *IEEE Trans. Plasma Sci.*, vol. 28, no. 3, pp. 478–484, Jun. 2000.

[8] M. C. Jones, V. B. Neculaes, Y. Y. Lau, R. M. Gilgenbach, and W. M. White, "Cathode priming of a relativistic magnetron," *Appl. Phys. Lett.*, vol. 85, no. 26, pp. 6332–6334, Dec. 2004.

[9] M. C. Jones *et al.*, "Magnetron priming by multiple cathodes," *Appl. Phys. Lett.*, vol. 87, no. 8, pp. 081501-1–081501-3, 2005.

[10] B. W. Hoff *et al.*, "Magnetic priming at the cathode of a relativistic magnetron," *IEEE Trans. Plasma Sci.*, vol. 36, no. 3, pp. 710–717, Jun. 2008.

[11] M. Fuks and E. Schamiloglu, "Rapid start of oscillations in a magnetron with a 'transparent' cathode," *Phys. Rev. Lett.*, vol. 95, pp. 205101-1–205101-4, Nov. 2005.

[12] M. I. Fuks and E. Schamiloglu, "70% efficient relativistic magnetron with axial extraction of radiation through a horn antenna," *IEEE Trans. Plasma Sci.*, vol. 38, no. 6, pp. 1302–1312, Jun. 2010.

[13] A. Sayapin, Y. Hadas, and Y. E. Krasik, "Drastic improvement in the *S*-band relativistic magnetron operation," *Appl. Phys. Lett.*, vol. 95, no. 7, pp. 074101-1–074101-3, 2009.

[14] A. Sayapin and A. Shlapakovski, "Transient operation of the relativistic S-band magnetron with radial output," *J. Appl. Phys.*, vol. 109, no. 6, pp. 063301-1–063301-5, 2011.

[15] M. Daimon and W. Jiang, "Modified configuration of relativistic magnetron with diffraction output for efficiency improvement," *Appl. Phys. Lett.*, vol. 91, no. 19, pp. 191503-1–191503-3, 2007.

[16] M. Daimon, K. Itoh, G. Imada, and W. Jiang, "Experimental demonstration of relativistic magnetron with modified output configuration," *Appl. Phys. Lett.*, vol. 92, no. 19, pp. 191504-1–191504-3, 2008.

[17] M. Liu, M. I. Fuks, E. Schamiloglu, and C. Liu, "Operation characteristics of A6 relativistic magnetron using single-stepped cavities with axial extraction," *IEEE Trans. Plasma Sci.*, vol. 42, no. 10, pp. 3344–3348, Oct. 2014.

[18] M. I. Fuks, S. Prasad, and E. Schamiloglu, "Efficient magnetron with a virtual cathode," *IEEE Trans. Plasma Sci.*, doi: 10.1109/TPS.2016.2525921.

[19] J. Benford and G. Benford, "Survey of pulse shortening in high-power microwave sources," *IEEE Trans. Plasma Sci.*, vol. 25, no. 2, pp. 311–317, Jun. 1997.

[20] W. Arter and J. W. Eastwood, "Characterization of relativistic magnetron behavior by 3-D PIC simulation," *IEEE Trans. Plasma Sci.*, vol. 26, no. 3, pp. 714–725, Jun. 1998.

[21] X. Chen, M. Esterson, and P. A. Lindsay, "Computer simulation of a high-power magnetron and the possible implications for RF pulse shortening," *IEEE Trans. Plasma Sci.*, vol. 26, no. 3, pp. 726–732, Jun. 1998.

[22] Y. Hadas, A. Sayapin, Y. E. Krasik, V. Bernshtam, and I. Schnitzer, "Plasma dynamics during relativistic *S*-band magnetron operation," *J. Appl. Phys.*, vol. 104, no. 6, pp. 064125-1–064125-7, 2008.

[23] J. G. Leopold, A. S. Shlapakovski, A. Sayapin, and Y. E. Krasik, "Revisiting power flow and pulse shortening in a relativistic magnetron," *IEEE Trans. Plasma Sci.*, vol. 43, no. 9, pp. 3168–3175, Sep. 2015.

[24] J. G. Leopold, A. Shlapakovski, A. Sayapin, and Y. E. Krasik, "A six vane, single radial output slot relativistic magnetron revisited," in *Proc. IEEE Pulsed Power Conf.*, Austin, TX, USA, May/Jun. 2015, pp. 1–6.

[25] H.-W. Chan, C. Chen, and R. C. Davidson, "Numerical study of relativistic magnetrons," *J. Appl. Phys.*, vol. 73, no. 11, pp. 7053–7060, 1993.

[26] B. Goplen, L. Ludeking, D. Smith, and D. Warren, "User-configurable MAGIC for electromagnetic PIC calculations," *Comput. Phys. Commun.*, vol. 87, nos. 1–2, pp. 54–86, May 1995.

[27] R. A. Stark, H. C. Chen, and H. S. Uhm, "Simulation studies of the relativistic magnetron," *Proc. SPIE*, vol. 1226, pp. 90–99, Apr. 1990.


Authors' photographs and biographies not available at the time of publication.